Applied Catalysis B: Environmental 321 (2023) 122065

Contents lists available at ScienceDirect

Applied Catalysis B: Environmental

journal homepage: www.elsevier.com/locate/apcatb

Membrane-free pure H_2 production over single dispersed Ru-anchored Pt_3Ni alloys via coupling ethanol selective electrooxidation

Chang-An Zhou [a], Shenghong Wang [a], Kui Ma [a], Lei Song [a], Lirong Zheng [c], Hairong Yue [a,b,*]

[a] Low-Carbon Technology and Chemical Reaction Engineering Laboratory, School of Chemical Engineering, Sichuan University, Chengdu 610065, China
[b] Institute of New Energy and Low-Carbon Technology, Sichuan University, Chengdu 610207, China
[c] Institute of High Energy Physics, Chinese Academy of Sciences, Beijing 100049, China

ARTICLE INFO

Keywords:
Ethanol
Electrooxidation
Selectivity
C2 pathway
Membrane-free H_2 generation

ABSTRACT

The sluggish kinetics and high overpotential of oxygen evolution reaction (OER) at anode hinders water splitting large-scale application. Recently, an anode alternative strategy exhibits promising prospect of application to improve reaction kinetics and decrease overpotential. Here, single dispersed Ru-anchored porous Pt_3Ni alloy (Ru_1-Pt_3Ni/NiF) were successfully synthesized via spontaneous galvanic reduction, over which highly selective electrooxidation of ethanol into acetate was realized. DFT calculations show that Ru modification introduced abundant active oxygen species (OH*), which not only enhanced the oxidation activity of ethanol, but also increased the selectivity for C2 oxidation pathway. Then a Ru_1-Pt_3Ni/NiF||Pt_3Ni/NiF ethanol oxidation membrane-free cell was built to couple the ethanol electrooxidation with H_2 evolution, where the Faraday efficiency of H_2 production reaches 94% and the power consumption is 19.24 kWh kg_{H2}^{-1}. This work provides a cost-competitive and energy-saving strategy for high-purity H_2 generation, opening new opportunities for electric energy utilization from renewable sources.

1. Introduction

Hydrogen is widely considered as a promising sustainable carbon-free energy carrier [1,2]. Although the traditional process of hydrogen generation from electrochemical water splitting is mature and has been commercialized, extremely high energy consumption of the overall water electrolysis owing to the sluggish reaction kinetics and high overpotential of the anodic oxygen evolution reaction [3]. In addition, a low-value anode product (O_2) and serious security issue due to risk of O_2 and H_2 leakage further hindered the large-scale commercialization of hydrogen production by water electrolysis. Currently, only 4% of the whole world total hydrogen produced by the water electrolysis. Due to the high overpotential required to yield appreciable current density, the power consumption in practical electrolyzers is nearly 1.5 ~ 2.2 times more than the theoretical case, with the actual energy efficiency is only about 60~80% in current commercial electrolyzers [4,5]. Hence, it is urgent and important to develop efficient catalysts and new hydrogen production reaction systems to lower the overpotentials, thus lowering the electricity consumption.

During the last decade, the strategy of electrochemical water splitting boosted by anodic chemical molecule oxidation reaction is undergoing fast development [4,6–10], which not only decreases the electrolysis voltage greatly by replacing anodic OER with a thermodynamically more favorable oxidation reaction with a low onset oxidation potential and fast reaction kinetics but also achieves value-added chemicals at the anode [11–13]. In addition, it can avoid the formation of O_2 or active oxygen species, improve the purity of cathode H_2 product, and reduce the purification cost of generating high-purity hydrogen, the security of process operation is also improved. For instance, Sun’s group [14] successfully realized the substitution of anode OER using the oxidation of 5-hydroxymethylfurfural to 2,5-furandicarboxylic acid at 3D Ni_2P nanoparticle arrays on nickel foam and simultaneously generation of H_2, 200 mV overpotential lower compared with pure water splitting. Zhang’s group [15] alternated anodic reaction with primary amine electrooxidation to accelerate H_2 production over NiSe nanorod, which not only boosted H_2 generation but also yielded valuable aromatic and aliphatic nitriles at the anode. Xia’s group [16] proposed the strategy of anodic hydrazine oxidation assists H_2 evolution over a $CoSe_2$ nanosheet, a cell voltage of 164 mV is required only to generate a current density of 10 mA cm^{-2} for stable water electrolysis.

* Corresponding author at: Low-Carbon Technology and Chemical Reaction Engineering Laboratory, School of Chemical Engineering, Sichuan University, Chengdu 610065, China.
E-mail address: hryue@scu.edu.cn (H. Yue).

https://doi.org/10.1016/j.apcatb.2022.122065
Received 8 June 2022; Received in revised form 3 October 2022; Accepted 6 October 2022
Available online 10 October 2022
0926-3373/

Recently, the electrochemical reforming of various alcohols has been widely investigated, such as methanol [9,17–21], ethanol [22–31], isopropanol [9,32], ethylene glycol [33], glycerol [34] and benzyl alcohol [13,35], showing the potential to be a low-cost and high-purity hydrogen production method. Profit from the favorable features of ethanol such as easy storage, transportation safety, low toxicity, high hydrogen content, and renewable from biomass, the electrochemical reforming of ethanol has become a competitive method for cost-saving H_2 generation. Noble metals (such as Pt [36–39], Pd [40–44], Rh [45,46] and Ir [47]) usually show high activity for EOR [48], regrettably, these noble metal-based electrocatalysts generally have strong ability for splitting C-C bond, which inevitably results in the generation of low-commercial value CO_2 (CO_3^{2-} in alkaline condition) during the EOR. Compared with the complete oxidation products of ethanol, the partial oxidation products (such as acetaldehyde and acetic acid) are value-added fine chemical products, which have a wide range of industrial applications, such as potassium acetate can serve as dehydrating agent, fiber treating agent, analytical reagent [25]. In addition, the generation of gaseous product can be avoided by controlling the selectivity of anodic reaction, so as to realize pure H_2 production without ion exchange membrane used. Thus, the rational design of EOR electrocatalysts with high selectivity, high activity and high stability to obtain value-added products and clean H_2 is of great significance.

Alloy effect is a general strategy to regulate the activity of EOR [26,27,45,49–51]. Due to the different properties of metal atoms, the addition of external metals may affect the electronic structure and geometric structure of the original atoms [52]. This electronic effect and stress effect will change the interaction between metals and intermediates or oxygen species (such as OH*), thus affecting the activity and selectivity of ethanol oxidation. Ruthenium, as an oxyphilic metal, can effectively increase the adsorption of oxygen species on the catalytic interface, thus enhancing the oxidation capacity of the catalysts and regulating reaction pathway [53]. In this work, we successfully synthesized single dispersed Ru-anchored porous Pt_3Ni alloy (Ru_1-Pt_3Ni) on nickel foam (NiF) via competitive reduction between Pt and Ru in the process of spontaneous galvanic reduction induced by electronegativity. Electrochemical tests showed that Ru_1-Pt_3Ni/NiF had high activity and selectivity for EOR in alkaline media, acetate was the only product detected during the ethanol oxidation reaction. DFT calculations showed that the introduction of Ru can significantly reduce the Gibbs formation energy of adsorbed hydroxyl and weaken the adsorption of acetic acid on the catalyst, thus enhancing the activity of ethanol oxidation and selectivity of acetic acid. When Ru_1-Pt_3Ni/NiF served as an anode EOR electrocatalyst in an ethanol oxidation membrane-free cell (2 M KOH + 2 M EtOH), only 0.7 V electrolysis voltage was required to reach 125 mA cm^{-2} current density for cathode H_2 generation, accompanying with 19.24 kWh kg_{H2}^{-1} unit power consumption.

2. Experimental section

2.1. Reagents

Chloroplatinic acid hexahydrate ($H_2PtCl_6 0.6\ H_2O$), Ruthenium chloride hydrate ($RuCl_3 \cdot xH_2O$) were purchased from Aladdin Co. Ltd. Pluronic F-127 were purchased from Sigma-Aldrich. Absolute ethanol and hydrochloric acid (HCl) were obtained from Kelong Chemical Co. Ltd. Commercial Pt loaded carbon paper (Pt loading, 1 mg cm^{-2}) were purchased from Hesen Co. Ltd. (Shanghai). All the chemicals used without further purification.

2.2. Fabrication of nickel-based electrodes

The nickel-based electrodes loading with platinum and ruthenium were prepared by the facile spontaneous reduction method. In a typical procedure, nickel foam (about 1.5 cm × 1 cm) was cleaned by 3 M HCl in an ultrasonic cleaner for 15 min to remove the surface impurities. Then the nickel foam was washed by ultrapure water and ethanol for several times, respectively, and blown dry under pure nitrogen. Meanwhile, H_2PtCl_6 (*x* mL, 20 mM), $RuCl_3$ (*y* mL, 20 mM), F127 (30 mg) and HCl (30 μL, 6 M) were mixed in a glass bottle under sonication for 30 min to ensure uniform dispersion. The cleaned nickel foam was immersed into the above solution at 25 °C for 12 h. After reaction, the obtained sample was washed with ultrapure water and ethanol to remove the residual reactants, then dried in pure nitrogen for further characterization and test. The obtained samples were denoted Pt_xRu_y/NiF, the *x* and *y* represent the volumes of Pt and Ru precursor solution added into the reaction solution, respectively. For comparison, pristine nickel-foam electrode was prepared by HCl treatment and ultrapure water wash.

2.3. Electrochemical measurements

Electrochemical tests were conducted on a CHI 660E electrochemical workstation. In a three-electrode configuration, the as-prepared Pt_xRu_y/NiF electrode, the Pt mesh electrode and a Hg/HgO electrode was used as the working electrode, the counter electrode and the reference electrode, respectively. Electrode potentials were converted into the reversible hydrogen electrode (RHE) scale using the equation E (RHE) = E (Hg/HgO) + 0.098 + 0.0592 *pH, where E (RHE) is the potential versus reversible hydrogen electrode and E (Hg/HgO) is the potential measured on Hg/HgO reference electrode. All the current density were normalized by the geometric area. The electrochemical EOR measurements were carried out in 40 mL of a 2 M KOH solution with 2 M ethanol at 25 °C. Before testing, the electrolyte solution was saturated with N_2 for 30 min. Linear sweep voltammetry (LSV) with a scan rate of 5 mV s^{-1} was conducted in 2 M ethanol with 2 M KOH solution. As a comparison, the EOR performance of Pt plate electrode and commercial carbon paper loaded Pt with the same size were measured under same conditions.

The overall splitting reaction was characterized using a two-electrode configuration in 2 M alcohol with 2 M KOH at a scan rate of 2 mV s^{-1}, the as-prepared $Pt_1Ru_{0.8}$/NiF and Pt_1/NiF used as anode and cathode respectively. The accelerated durability tests of the catalysts were performed in the N_2 saturated 1 M ethanol electrolyte with 1 M KOH at room temperature (25 °C) by applying potential cycling between − 0.12 V and 0.45 V vs RHE at a sweep rate of 50 mV s^{-1} for 1000 cycles. The chronoamperometry curve obtained in a two-electrode configuration with constant cell voltage of 0.5 V. Electrochemical impedance spectroscopy (EIS) measurements were carried out on PARSTAT 4000^+ in 1 M KOH with 1 M EtOH at 0.6 V in a frequency range of 0.5 Hz to 10^5 Hz with an AC voltage amplitude of 10 mV.

The double-layer capacitance (C_{dl}) method was used to evaluate the electrochemical active surface area (ECSA). It is widely accepted that the ECSA is linearly proportional to the double-layer capacitance in non-faradaic range, which can be derived from the CV cycles tests at different scan rates in the range of 0.075–0.175 V vs. RHE, where there is no Faradic current. The ECSA was calculated according to the equation of ECSA = C_{dl}/C_s, the C_{dl} is the double-layer capacitance of the working electrode and the C_s is the specific capacitance value for a flat standard with 1 cm^2 of real surface area. Specific capacitances have been measured for a variety of Pt and Ni electrodes in alkaline solutions and typical values reported range between $C_s = 25 \sim 60$ μF cm^{-2} in NaOH and KOH solutions[54–58]. For Pt_3Ni (111) single crystal, C_s was specified as the average specific capacitances for these Pt and Ni-containing materials (36.6 μF cm^{-2}).

A sealed and membrane-free total electrolysis system was built for energy consumption evaluation of ethanol selective oxidation coupling hydrogen production, the as-prepared $Pt_1Ru_{0.8}$/NiF (1 cm^2) and Pt_1/NiF (1 cm^2) used as anode and cathode respectively with the distance between electrodes at 15 mm. The electrochemical reforming was performed in an aqueous mixture of 2 M KOH + 2 M ethanol and the working current density was set at 125 mA cm^{-2}. The generated hydrogen was collected and quantified by mass spectrometry. The Faraday efficiency (FE) was calculated according the equation of FE (%)

$= n_E/n_T \times 100\%$, where the n_E represents the experimental amount of H_2 detected by mass spectrometry, n_T is the theoretical amount of H_2 was calculated by Faraday's law.

2.4. Materials characterization

The X-ray diffraction (XRD) patterns were recorded on a DX-2700 (Dandong Haoyuan) instrument equipped with Cu Kα radiation (k = 0.15418 nm) in the 2θ range of 20–90°, the scan step of 0.03° and accumulation time of 0.5 s were adopted. The surface morphology of samples were observed by scanning electron microscopy (SEM) on a JEOL 7610 F instrument at 15.0 kV. Transmission electron microscopy (TEM) was measured on Tecnai G2 F20 S-TWIN (FEI). Aberration correction scanning transmission electron microscope (AC-STEM) was conducted on FEI Titan Themis 60–300. X-ray photoelectron spectra (XPS) were carried out on an Escalab 250Xi (Thermo Fisher Scientific) using Al Kα radiation. The content of Pt and Ru were obtained via inductively coupled plasma-optical emission spectrometer (ICP-OES) (Agilent 720).

2.5. X-ray absorption spectroscopy (XAS) measurements

XAFS spectra data for Ru K-edge and Pt L_3-edge were collected at the 1W1B station in the Beijing Synchrotron Radiation Facility (BSRF, operated at 2.5 GeV with a maximum current of 250 mA). In order to obtain high quality oscillation signal for the coordination structure analysis, Pt L_3-edge and Ru K-edge data of $Pt_1Ru_{0.8}$/NiF sample were collected in fluorescence mode using a sixteen-element Ge detector. For other samples, the Pt L_3-edge and Ru K-edge data were collected in fluorescence mode using a Lytle detector at room temperature.

In situ XAFS measurements were conducted to obtain the change of valence state and coordination environment for elemental analysis during the reaction. The in situ XAFS spectra were collected in the potentiostatic mode on a home-made electrochemical cell. $Pt_1Ru_{0.8}$/NiF used as the working electrode, Pt wire as the counter electrode and a Hg/HgO electrode as the reference electrode, N_2 purged 1 M CH_3CH_2OH with 1 M KOH solution used as electrolyte.

2.6. In situ FTIR spectroscopy measurements

In situ infrared reflection-absorption spectroscopy (IRRAS) measurements were performed using a Thermo Fisher IS 50 spectrometers equipped with MCT detector. All experiments were carried at room temperature on a homemade three-electrode in situ cell which is equipped with a CaF_2 window, a Hg/HgO reference electrode, a Pt wire counter electrode and an Au electrode with a geometric area of 0.196 cm^2 as the current collector. The working electrode was prepared by replacing the nickel foam in the above preparation method into nickel foil with a diameter of 1 cm. A 1 M solution of KOH with 1 M CH_3CH_2OH was used as electrolyte and was purged with N_2 before measurement. To identify the intermediates and products of EOR dependent on potential, spectra were collected from 0.1 V to 1.0 V (vs. RHE) in a 0.1 V interval. In the potentiostatic mode, each potential was maintained for 120 s, during which the infrared spectra were collected. The resolution of all IR spectra was set to 8 cm^{-1} and 64 interferograms were co-added to each spectrum. The IR spectra were calculated for each potential as differential spectrum relative to a reference single-beam spectrum (R_{ref}) taken at 0 V vs RHE as follows: A = -lg (R_E/R_{ref}), where the R_E and A is the single-beam spectrum at different potential and the absorbance, respectively. According to the definition, the downwards bands indicated a decrease in concentration or the consumption of species with respect to the reference potential. Meanwhile, the upwards bands corresponded to an increase in concentration or the generation of species. ATR (Attenuated Total Reflectance) infrared spectroscopy for several possible products of the EOR were recorded in 1 mol L^{-1} KOH solution for reference.

2.7. DFT computational methods

Density functional theory (DFT) calculations were performed with the Vienna Ab-initio Simulation Package (VASP) [59,60]. The generalized gradient approximation of Perdew, Burke, and Erzenhorf (PBE) was used to compute the exchange-correlation energy. The projected augmented wave (PAW) method was employed to describe the core-electron interaction [61]. The cut-off energy was set to 450 eV. The Ru doped Pt_3Ni (111) surfaces were modeled by a periodic slab with p (4 × 4) supercell of 4 layers and a vacuum region of 15 Å. A 5 × 5 × 1 Monkhorst-Pack k-points mesh was employed for the Brillouin zone integration. Only the top two layers were allowed to relax while the bottom two layers were kept fixed during all the geometry optimization. The convergence threshold of energy for the iteration in self-consistent field (SCF) was set at 10^{-6} eV and that of forces for geometry optimizations was set to 0.02 eV/Å. Spin-polarization was included for both surfaces.

In this work, the adsorption energy was defined as: $\Delta E_{ad} = E_{(ad+slab)} - E_{ad} - E_{slab}$, where $E_{(ad+slab)}$, E_{ad} and E_{slab} is the total energies of the adsorbate biding to slab, free adsorbate in gas phase and clean slab, respectively. The free energy of species was obtained from $G = E + ZPE - TS$, where E is the total energy of species, ZPE is the zero point energy and S is the entropy at 298 K. Because it is difficult to obtain the exact free energy of OH^- in the electrolyte solution, the adsorption free energy ΔG_{OH} are relative to the free energy of stoichiometrically appropriate amounts of H_2O (g) and H_2 (g), defined as follows:

$$OH^- + * \rightarrow OH* + e^- \quad (1)$$

By setting the reference potential to standard hydrogen electrode, we can relate the chemical potential for the reaction ($H^+ + e^-$) to that of 1/2 H_2. That means the Eq. 1 is equivalent to:

$$OH^- + H^+ + * \rightarrow OH* + 1/2\ H_2\ (g) \quad (2)$$

The term of ($OH^- + H^+$) on the left side of Eq. 2 can be calculated by the free formation of Eq. 3 (ΔG_3):

$$OH^- + H^+ \rightarrow H_2O \quad (3)$$

So, the adsorption free energy ΔG_{OH} can be calculated according following equation:

$$\Delta G_{OH} = G_{OH*} + 1/2\ G_{H2} - G* + \Delta G_3 - G_{H2O} \quad (4)$$

ΔG_3 refer to the experiment data [62], the ZPE and S were calculated by vaspkit.1.2.1[63].

3. Results and discussion

3.1. Synthesis and characterization of catalysts

Monodisperse Ru-anchored Pt_3Ni/Ni-foam catalysts were prepared by competitive reduction between Pt and Ru in the process of galvanic spontaneous reduction, the detailed preparation procedure is presented in Fig. 1a. As shown in Table S1, the standard potential in respect to standard hydrogen electrode (SHE) of the reduction of $[PtCl_6]^{2-}$ to $[PtCl_4]^{2-}$ and $[PtCl_4]^{2-}$ to Pt is 0.680 and 0.755 V, respectively. However, the standard potential for Ru^{3+} reduction to Ru^{2+} and Ru^{2+} to Ru is 0.240 and 0.455 V. Due to the more negative standard reduction potential (−0.257 eV) of Ni compared with Pt and Ru, the metallic Ni can form spontaneous redox pairs with the $[PtCl_6]^{2-}$ and Ru^{3+} ions in precursor solution. Due to the more positive standard reduction potential of $[PtCl_6]^{2-}$ than that of Ru^{3+}, contributes in faster reduction kinetics of $[PtCl_6]^{2-}$ than Ru^{3+}, the oxidized $[PtCl_6]^{2-}$ and $[PtCl_4]^{2-}$ ions in solution are reduced prior to Ru^{3+}. In addition, it is thermodynamical feasible that the reduced metallic Ru can be oxidized by $[PtCl_6]^{2-}$ and $[PtCl_4]^{2-}$ ions in the solution and re-dissolved into the solution, which may make only a few Ru atoms remain in the reduced metal alloy phase, and the

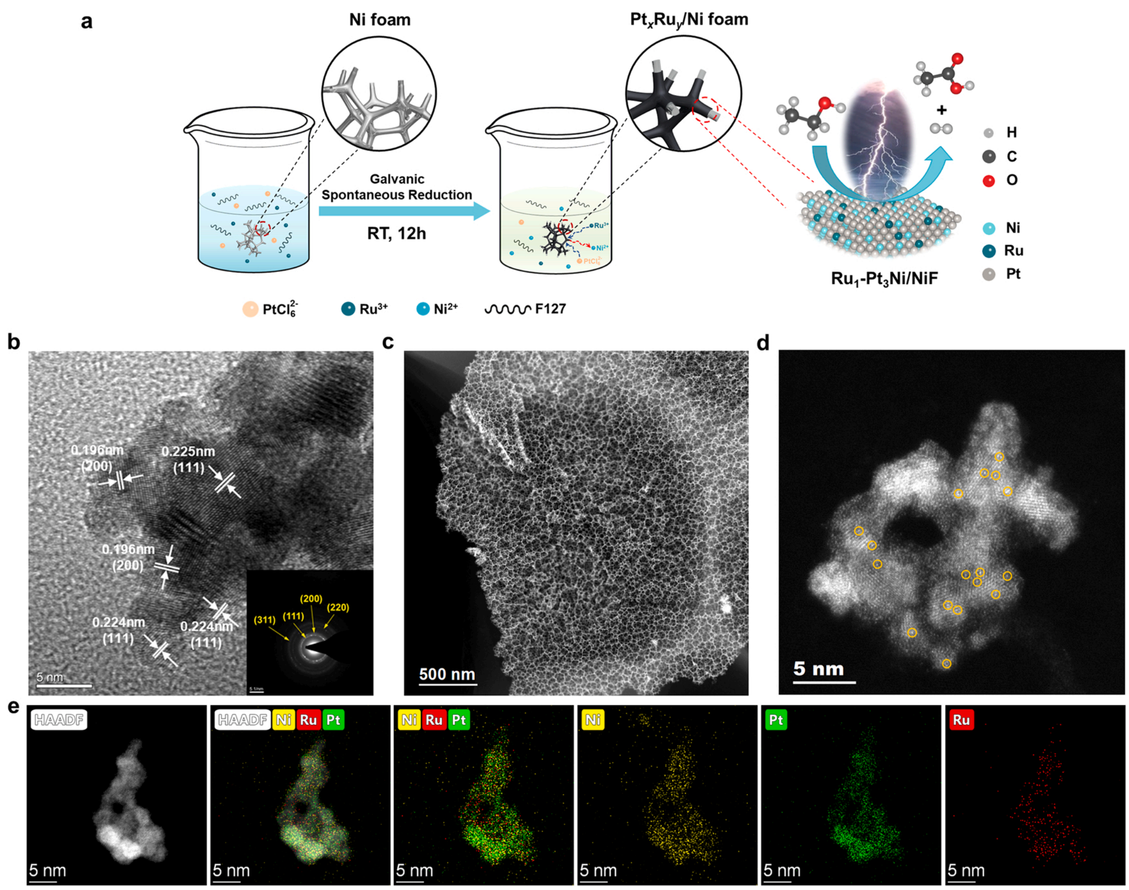

Fig. 1. Morphological and structural characterization of Ru_1-Pt_3Ni/NiF samples. (a) Illustration of Ru_1-Pt_3Ni/NiF formation through a spontaneous galvanic reduction process. (b) HRTEM image of Ru_1-Pt_3Ni/NiF. Insets in panels b is the selected area electron diffraction (SAED) pattern of Ru_1-Pt_3Ni/NiF showing the facet-centered cubic lattice structure. (c) TEM image of Ru_1-Pt_3Ni/NiF with porous structure. (d) High angle annular dark-field scanning transmission electron microscope (HAADF-STEM) image. (e) STEM-EDS elemental mapping of a representative single Ru_1-Pt_3Ni/NiF present the distribution of Ni (yellow), Pt (green) and Ru (red).

residual Ru atoms can even exist in monodisperse. The X-ray diffraction (XRD) pattern of Pt_1/NiF without Ru doping showed peaks at 40.3° and 46.8°, corresponding to the (111) and (200) planes of Pt_3Ni alloy (Fig. 2e). The peaks at 44.6°, 52.0° and 76.6° belong to Ni foam framework. The sample was marked as Pt_3Ni/NiF. SEM images showed the nickel skeleton was wrapped by a layer of ~ 300 nm thin film, the film with micropores was formed by accumulation of nanoparticles (Fig. S1). Ordered alloy phases can be observed in high magnification TEM image and corresponding selected area electron diffraction (SAED) pattern of Pt_3Ni/NiF sample (Fig. S4d). Furthermore, well-resolved lattice fringes with an interplanar distance of 0.224 nm in the HRTEM image of Pt_3Ni/NiF (Fig. S4c), also indicated that $PtCl_6^{2-}$ was reduced to form Pt_3Ni alloy on the nickel foam skeleton during galvanic redox replacement reaction. Ru-anchored Pt_3Ni/Ni-foam samples (the $Pt_1Ru_{0.8}$/NiF sample) showed identical diffraction peak in the XRD pattern compared with Pt_3Ni/NiF, except the broadening of Pt_3Ni alloy (111) plane diffraction peak (Fig. 2e), and no formation of Ru nanoparticles was observed in HRTEM image of Ru-anchored Pt_3Ni/Ni-foam (Fig. 1b). The doping of Ru decreases the crystal size of Pt_3Ni according to the calculation of Scherrer formula, but does not change the alloy phase structure, which is consistent with the statistical results of average size distribution (form 3.94–2.58 nm) (Figs. S4,5). TEM image exhibits that Ru-doped Pt_3Ni forms homogeneous porous structure (Fig. 1c), it greatly increases the specific surface area of the catalyst and helps to provide more catalytic reaction sites for the electrooxidation of ethanol. In addition, Ru-doped samples showed more compact film compared with Pt_3Ni/NiF (Fig. S2), which means the catalyst layer is more difficult to exfoliate from the nickel substrates and more stable. Direct evidence for the presence of Ru single atoms is obtained via aberration corrected scanning transmission electron microscopy (AC-STEM) (Fig. 1d), the single Ru atoms were uniformly dispersed on the (111) lattice plane of Pt_3Ni nanoparticles (noted as Ru_1-Pt_3Ni/NiF henceforth). Energy-dispersive x-ray spectroscopy (EDS) elemental mapping in a scanning transmission electron microscope (STEM) revealed that atomic Ru was evenly dispersed in Pt_3Ni nanoparticles (Fig. 1e).

To further investigate the electronic structure of Ru-doped Pt_3Ni/NiF catalyst and demonstrate atomic dispersion of Ru species, X-ray absorption near-edge structure (XANES) and extended X-ray absorption fine structure (EXAFS) were conducted to provide valence state and local coordination information of Pt and Ru central atoms, and typical results of the Pt_3Ni/NiF doped Ru were shown in Fig. 2a-d, S6. The valence state of Pt can be probed by the white line intensity of Pt L_3-egde in XANES spectra. The Pt L_3-edge XANES results showed that the white line intensity of is close to Pt foil and decline gradually with the increase of Ru contents in the catalyst, indicating that the average valence state of Pt is mostly zero and there is an electron transfer from ruthenium to platinum (Fig. S7). Further X-ray photoelectron spectroscopy (XPS) characterization revealed the Pt^0 and $Pt^{\delta-}$ (Pt species of negative valence) coexist in our catalysts (Fig. 2 f). The peaks at 70.6 eV and 74.0 eV can be assigned to 4 $f_{7/2}$ and 4 $f_{5/2}$ of $Pt^{\delta-}$ species, and the peaks at 71.3 eV and 74.6 eV belong to Pt^0. The binding energy of Pt 4 f in Ru-doped Pt_3Ni/NiF has a negative shift about 0.1 eV compared to Pt_3Ni/NiF, which also proved the electron donation from ruthenium to platinum. XANES for the Ru K-edge suggested that the ruthenium species have an average oxidation state between Ru foil and RuO_2 bulk according to the absorption edge position and white line intensity

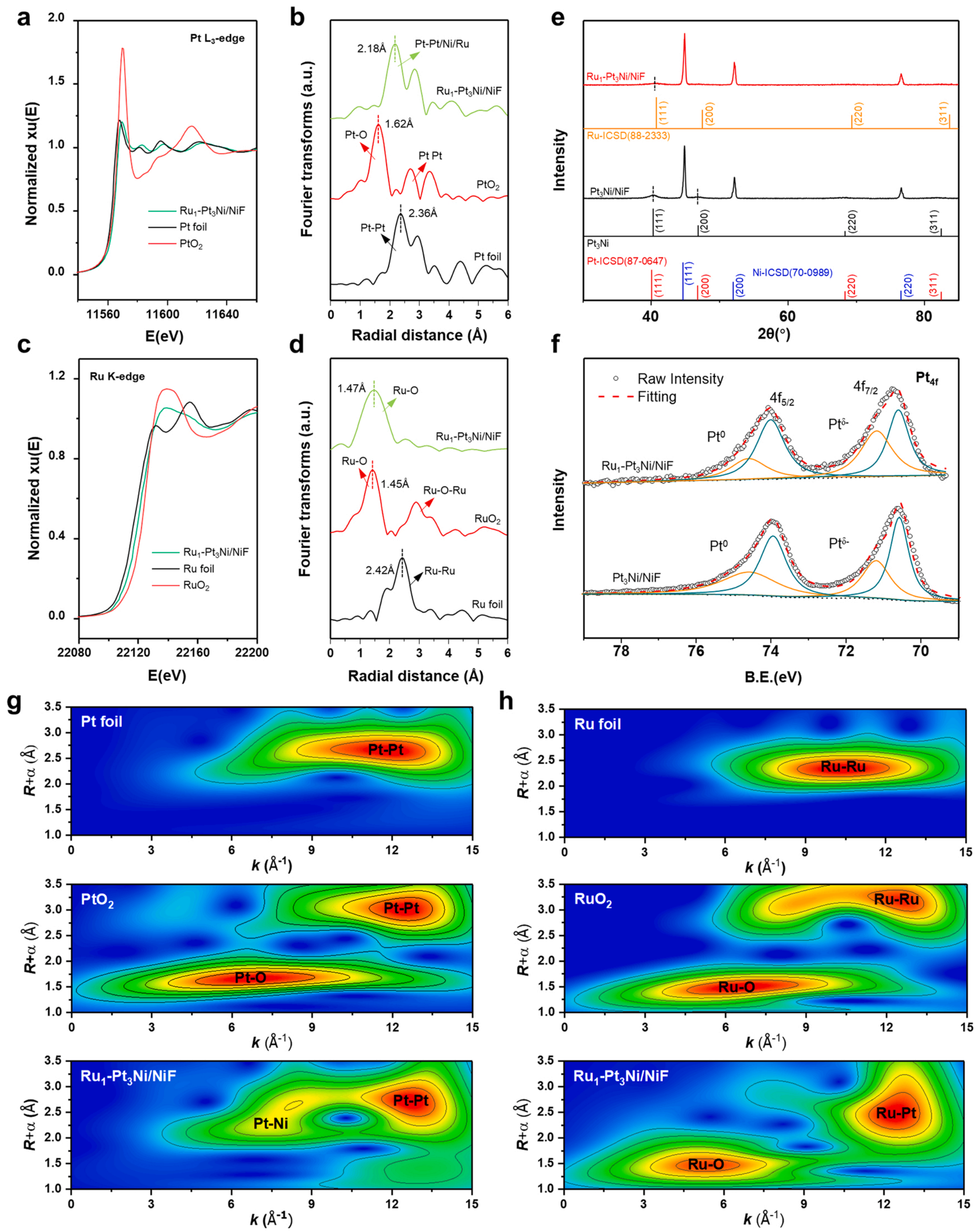

Fig. 2. X-ray characterization of Ru_1-Pt_3Ni/NiF samples for Pt and Ru. XANES spectra of (a) Pt L_3-edge and (c) Ru K-edge for Ru_1-Pt_3Ni/NiF. The k^2-weighted R-space FT-EXAFS spectra of (b) Pt L_3-edge and (d) Ru K-edge for Ru_1-Pt_3Ni/NiF and standard samples (Pt foil, PtO_2, Ru foil and RuO_2). (e) The XRD patterns of Ru_1-Pt_3Ni/NiF and Pt_3Ni/NiF. (f) XPS patterns of Pt 4 f orbit for Pt_3Ni/NiF and Ru_1-Pt_3Ni/NiF. (g) Pt L_3-edge wavelet transforms for k^3-weighted EXAFS spectra of Ru_1-Pt_3Ni/NiF, PtO_2 and Pt foil. (h) Ru K-edge wavelet transforms for k^3-weighted EXAFS spectra of Ru_1-Pt_3Ni/NiF, RuO_2 and Ru foil.

(Fig. 2c), which further confirms the electron loss of ruthenium species. In addition, Ru-doped Pt_3Ni/NiF shows the binding energy of Ru $3p_{3/2}$ and Ru $3p_{1/2}$ at 461.8 eV and 484.7 eV (Fig. S19b), respectively, which is higher than Ru^0 and lower than Ru^{3+}.

The Pt L_3-edge Fourier transform (FT) of EXAFS spectra shows a main peak at ~ 2.18 Å, which is shorter than the Pt-Pt coordination peak in bulk Pt (~ 2.36 Å in Pt foil) (Fig. 2b). It proved that there are shorter Pt-Ni or Pt-Ru bonds in crystalline phase due to some of the Pt atoms around Pt central atom are substituted by Ni and Ru with smaller atomic radius. The Ru K-edge FT-EXAFS spectra show that one single scattering peak appeared at 1.47 Å belongs to the scattering of Ru-O coordination shell in the Ru-doped Pt_3Ni/NiF sample, while the peaks attributed to the Ru-Ru bonds and Ru-O-Ru coordination are almost indiscernible (Fig. 2d). The absence of Ru-Ru bonds (at 2.42 Å) and related Ru-O-Ru scattering path at second coordination shell denies the existence of metallic Ru clusters and RuO_2 particles. Combining with AC-STEM results, further supports the hypothesis that Ru species exist as atomic dispersed inside the Pt_3Ni/NiF.

To visually reveal the coordination environment around Pt and Ru in the catalyst, the EXAFS spectra were conducted wavelet transform (WT) analysis. Due to the high resolution in both radial distance and the *k*-space, WT-EXAFS analysis is sensitive to the atomic number of elements, and can distinguish the back-scattering atoms of light elements, even if they are obviously overlapped in R-space. Fig. 2g, h shows the Pt L_3-edge and Ru K-edge WT contour plots of Ru_1-Pt_3Ni/NiF based on the Morlet wavelets, with optimized parameters of $k = 8$ and $\sigma = 1$. The Pt L_3-edge WT intensity maximum of Ru_1-Pt_3Ni/NiF and Pt foil both located at *R* space of ~2.7 Å and *k* space of 12–12.7 $Å^{-1}$, confirming the similar coordination structure of Pt-Pt bonds like Pt foil. Different from the Pt-O bonds in PtO_2 standard sample appeared maximum intensity at ~ 1.6 Å and 7 $Å^{-1}$, a new WT intensity maximum occurred near 2.4 Å and 7.5 $Å^{-1}$, which was associated with Pt–Ni/Ru bonding. This result is consistent with the conclusion that the main phase of the catalyst is Pt_3Ni alloy. For the WT spectra of Ru K-edge, similar intensity maximum appeared near 1.5 Å in *R* space and 6 $Å^{-1}$ in *k* space both in Ru_1-Pt_3Ni/NiF and RuO_2, which is contributed by the Ru-O bond in the first coordination shell. However, the intensity maximum near 2.5 Å in R space of the Ru_1-Pt_3Ni/NiF is different with that of RuO_2 appeared at 3.2 Å, which indicates that the absence of Ru-O-Ru coordination structure in the second shell and Ru in the catalyst does not exist in the form of RuO_2. Compared with the Ru foil standard sample, we propose that it is contributed by the backscattering of the Ru central atom and the surrounding Pt/Ni atom.

3.2. Electrochemical activity for EOR

The EOR activities of Ru_1-Pt_3Ni/NiF were evaluated in a three-electrode system containing 2 M KOH and 2 M ethanol. LSV was used to investigate the performance of the Ru_1-Pt_3Ni/NiF, and the results were compared with those for the Pt/C and Pt plate electrode under the same test conditions. The geometric-normalized LSV curve shows a current density of 350 mA cm^{-1} at 0.6 V vs. RHE (Fig. S8), more than five times compared with the commercial Pt/C (62 mA cm^{-1} with 1 mg_{Pt} cm^{-2}). Furthermore, the mass activity of EOR for Ru_1-Pt_3Ni/NiF ($Pt_1Ru_{0.8}$/NiF) at potential of 0.6 V vs. RHE is 0.22 A mg_{Pt}^{-1} by normalizing to the Pt loading (Table S2), which is three times greater than that of the commercial Pt/C catalyst (1 mg_{Pt} cm^{-2}, 0.05 A mg_{Pt}^{-1}). Additionally, a 65 mV decrease in the onset potential (defined as the potential required to reach to a current density of 10 mA cm^{-1}) is observed in the Ru_1-Pt_3Ni/NiF when compared with Pt/C, suggesting the lower activation barrier of ethanol oxidation on the Ru_1-Pt_3Ni/NiF surface (Fig. S8).

At the same time, the EOR performance of catalysts with different Pt/Ru ratio was also investigated. Samples only loaded with ruthenium (Ru_1/NiF) show negligible electrochemical activity (Fig. 3a), however, samples only loaded with platinum (Pt_1/NiF) shows good EOR activity and the activity enhanced with the doping of ruthenium (Fig. 3b). Because of the formation of a Ru-rich sites in Ru_1/NiF sample, the high oxophilicity of Ru surface atoms decreases the ethanol adsorption, resulting in a lower EOR activity. For the samples loaded with Pt and Ru simultaneously (Pt_xRu_y/NiF), the previous characterization shows the Ru exists on the surface of Pt_3Ni alloy in the form of single disperse atom, in which the Pt provides sites for ethanol and intermediates adsorption, and the neighboring Ru provides sites to produces oxygen species for the oxidation of intermediates adsorbed on the neighboring Pt sites. This synergetic effect greatly enhances the EOR activity of Ru_1-Pt_3Ni/NiF catalysts. Sample of $Pt_1Ru_{0.2}$/NiF gives the smallest Tafel slope of 126.1 mV per decade, which is smaller than both Pt plate electrode (305.3 mV dec^{-1}) and commercial Pt/C electrode (145.8 mV dec^{-1}) (Fig. 3c), and samples of $Pt_1Ru_{0.8}$/NiF give the lowest onset potential with the similar Tafel slope (146.7 mV dec^{-1}) to commercial Pt/C (Table S3). Combining with the ICP-OES results (Table S2) and LSV tests

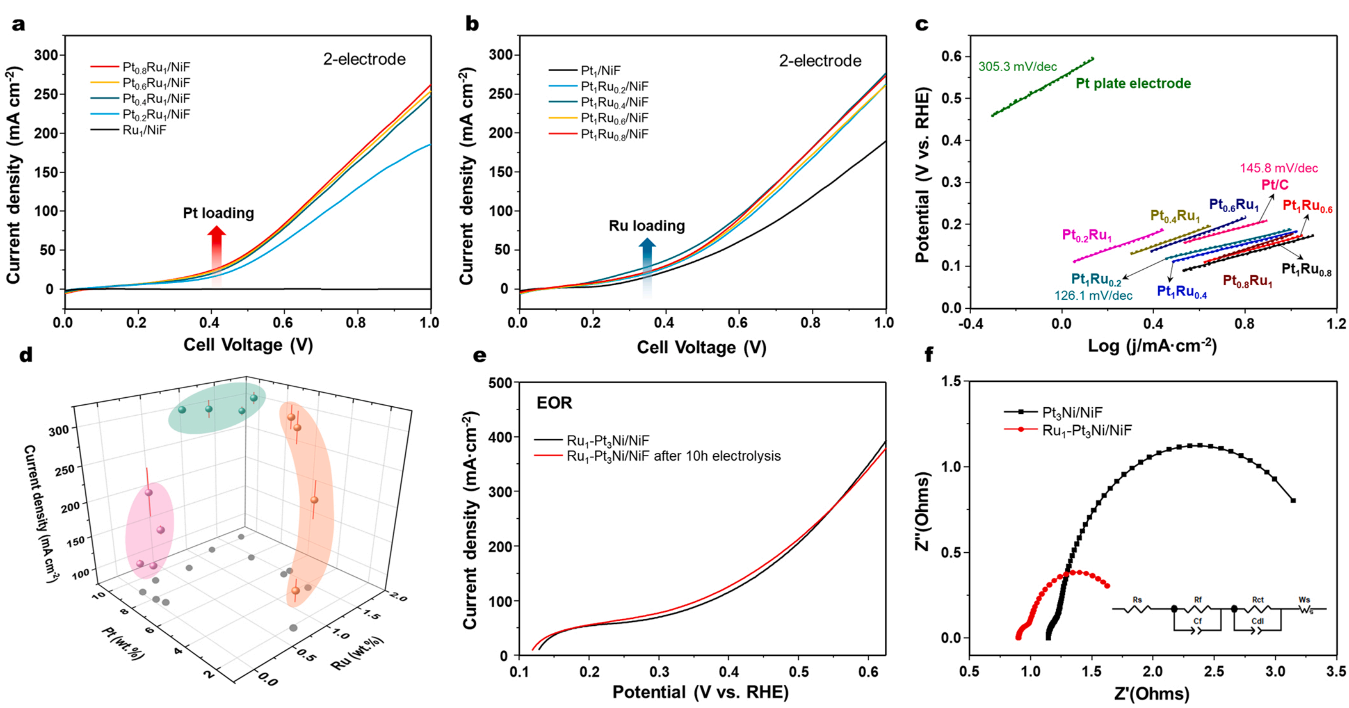

Fig. 3. The electrochemical performance investigations of Ru_1-Pt_3Ni/NiF during the EOR process. (a, b) J-V curves of Ru_1-Pt_3Ni/NiF with different PtRu ratio in 2 M EtOH solutions within 2 M KOH measured at 25 ℃. (c) Tafel plots for different anodes measured at 2 mV s^{-1}. (d) The EOR current density of electrocatalysts with different Pt and Ru loading at 0.6 V vs. RHE on anode. The violet spheres represent samples of $Pt_1Ru_{0.01}$/NiF, $Pt_1Ru_{0.02}$/NiF, $Pt_1Ru_{0.05}$/NiF, $Pt_1Ru_{0.1}$/NiF; green spheres represent samples of $Pt_1Ru_{0.2}$/NiF, $Pt_1Ru_{0.4}$/NiF, $Pt_1Ru_{0.6}$/NiF, $Pt_1Ru_{0.8}$/NiF; brown spheres represent samples of $Pt_{0.2}Ru_1$/NiF, $Pt_{0.4}Ru_1$/NiF, $Pt_{0.6}Ru_1$/NiF, $Pt_{0.8}Ru_1$/NiF. The error bars represent the decay of EOR electrocatalytic activity. (e) EOR polarization curves of pristine and aged Ru_1-Pt_3Ni/NiF in a three-electrode configuration with scan rates of 5 mV s^{-1}. (f) EIS data fitting result of 1 M EtOH with 1 M KOH over a frequency range of 0.5 Hz to 10^5 Hz with an AC voltage amplitude of 10 mV. The insert diagram is the fitting circuit.

(Fig. S9, S10) of different Pt/Ru ratio samples, we can observe that the stability of catalysts is poor when the mass ratio of Pt/Ru is less than 4 (brown shadow area in Fig. 3d), although it shows high mass activity (Fig. S11). However, in the samples with high Pt/Ru mass ratio (higher than 35, purple shadow area in Fig. 3d), the mass activity is barely satisfactory due to the lack of sufficient Pt-Ru adjacent sites. Catalysts exhibit high mass activity and stability when the mass ratio of Pt/Ru in the interval of 12.5 ~ 5.5 (green shadow area in Fig. 3d).

To further study the catalytic kinetic characteristics of the catalysts, electrochemical impedance spectroscopy (EIS) was conducted at 0.6 V vs. RHE over a frequency range of 0.5 Hz to 10^5 Hz in 1 M KOH with 1 M ethanol. The small charge transfer resistance (R_{ct}) value of 0.68 Ω for the Ru_1-Pt_3Ni/NiF, significantly lower than 2.24 Ω of Pt_3Ni/NiF, indicates that the doping of Ru enhanced the electrons transfer at the Ru_1-Pt_3Ni/NiF and electrolyte interface of the ethanol oxidation reaction (Fig. 3f). The excellent EOR performance of Ru dope Pt_3Ni/NiF catalysts can also be attributed to large double layer capacitance (~306 mF cm^{-2}) and high ECSA (0.838 m^2 $cm^{-2}_{eletrode}$), which are derived from cyclic voltammetry diagrams under different scan rates (Fig. S12-14). CV curves in 1 M KOH are shown in Fig. S15, with the increasing of Ru loading, the double layer capacitance of catalysts increased significantly, and the formation potential of OH_{ads} species decreased, thus the enhancement of ethanol oxidation activity is attributed to more surface-active sites and more easily formed surface oxygen species by Ru doping.

In addition, the XRD and XPS patterns of Ru_1-Pt_3Ni/NiF after the electrochemical measurements were consistent with the fresh samples, which indicated the stability of the crystal structure and electronic structure of catalysts (Fig. S16,17). CV curves were also performed to evaluate the stability of Pt_3Ni/NiF and Ru_1-Pt_3Ni/NiF in EOR. Apparently, the EOR activity of the Pt_3Ni/NiF catalyst shows a ~28% decay after 1000 CV test at 0.45 V vs. RHE, and the HER activity shows a ~16% decline at 0.15 V vs. RHE (Fig. S18b). In contrast, the Ru_1-Pt_3Ni/NiF shows a relatively stable EOR activity and an increased HER activity after 1000 CV test under the same conditions (Fig. S18a), clearly demonstrating the superior stability of Ru_1-Pt_3Ni/NiF catalysts when compared to Pt_3Ni/NiF. The polarization curves (Fig. 3e) and chronoamperometry tests (Fig. S19) further confirm the stability of Ru_1-Pt_3Ni/NiF catalyst for EOR. These studies demonstrate that the doping of Ru not only boosts the EOR activity, but also improves the durability.

In order to investigate the power consumption and stability of hydrogen production by electrochemical reforming of ethanol, a reforming cell consist of Ru_1-Pt_3Ni/NiF anode and Pt_3Ni/NiF cathode was built. The stability of the electrolyzer cell was tested on the electrochemical workstation using a two-electrode system at 125 mA cm^{-2} current density, and the potential of the electrolyzer cell was about 0.7 V (Fig. S20). In a single test (0.5 h), the Faraday efficiency of hydrogen production reaches 94%, and the power consumption per unit mass of H_2 is 19.24 kWh (Table S5). The decrease of Faraday efficiency in subsequent tests may be due to the reduction of partial oxidized intermediate species at the cathode and the decay of Pt_3Ni/NiF cathode HER activity (Fig. S21). Comparison of reaction temperatures, cell voltage, current density and power consumption for H_2 production via alcohols electro-reforming reported in this work and the literatures were listed in Table 1. The electrooxidation activity of other common biomass alcohols (methanol, ethylene glycol and glycerol) were also evaluated (Fig. S22), the cathode can also generate hydrogen efficiently, but the oxidation efficiencies of EG and glycerol are lower than that of methanol and ethanol.

3.3. *In situ FTIR experiments analysis*

Chronoamperometry measurements were coupled with in situ FTIR to identify ethanol electro-oxidation products at different potentials and investigate the reaction mechanism. In order to determine the infrared vibrational frequencies of the characteristic functional groups, we measured the attenuated total reflection spectra of several possible intermediates in EOR. ATR spectra obtained in 1 M KOH solution and standard samples for several possible products of the EOR were shown in Fig. S23, 24. The major band between 1550 cm^{-1} and 1700 cm^{-1} belongs to the bending vibration of hydroxyl group in water. The C-O stretching vibration in ethanol is located at 1045 cm^{-1}. Two bands at 1550 cm^{-1} and 1414 cm^{-1} attributed to asymmetric and symmetric C-O bonds stretching vibrations characteristic of acetate ions (CH_3COO^-). Considering that acetaldehyde is prone to self-polymerization, the ATR spectrum of acetaldehyde is complex, and difficult to assign the vibration bands. According to the report by Neto and F.J. Rodríguez et al. [30, 73], the band at 1346 cm^{-1} may be attributed to acetaldehyde (CH_3CHO).

Fig. 4a, b shows the IR spectra obtained during the EOR for the different studied catalysts under different oxidation potential. For both Ru_1-Pt_3Ni/NiF and Pt_3Ni/NiF catalysts, the characteristic vibration peaks of CH_3COO^- (at 1550 cm^{-1} and 1414 cm^{-1}) and CH_3CHO (at 1346 cm^{-1}) become more intense as the potential increase, while an increase in the consumption of CH_3CH_2OH occurs as indicated by the bands at 1044 cm^{-1}. This characteristic indicates that ethanol was gradually consumed and acetaldehyde and acetic acid were formed during the EOR process. Finally, acetic acid is neutralized by OH^- to form acetate ions. It should be noted that no obvious CO (~2180 cm^{-1}) and CO_3^{2-} (~1380 cm^{-1}) vibration peaks were observed in the spectra during this process, even at quite high potentials (1 V vs. RHE). Considering that the infrared characteristic peak frequency of carbonate (~1380 cm^{-1}) is close to that of acetate (1414 cm^{-1}), a weak carbonate signal generated by ethanol oxidation is easily overlapping with the main product acetate, the oxidation products of ethanol were further

Table 1
Performance comparison of alcohol electrooxidation couple with H_2 generation.

Electrolyte	Temperature (°C)	Cell voltage (V)	Current density (A cm^{-2})	Power consumption (kWh kg^{-1})	Reference
1 M CH_3OH/H_2O solution[a]	70	0.67	0.3	17.8	[64]
4 M CH_3OH/H_2O solution[a]	80	0.79	0.2	23.0	[65]
2 M CH_3OH[a]	60	0.80	0.3	21.3	[66]
6 M C_2H_5OH/H_2O solution[a]	80	1.1	0.25	31.9	[23]
2 M C_2H_5OH + 0.5 M H_2SO_4[a]	20	0.90	0.10	28.0	[67]
2 M C_2H_5OH/H_2O solution[a]	70	0.75	0.20	19.7	[68]
2 M C_2H_5OH + 2 M NaOH[a]	80	0.70	1.0	24.0	[69]
6 M C_2H_5OH/H_2O solution[a]	80	1.0	0.192	27.0	[69]
2 M C_2H_5OH + 2 M KOH[a]	60	1.0	0.05	19.3	[70]
2 M C_2H_5OH + 2 M KOH[a]	60	0.70	0.49	9.60	[71]
2 M C_2H_5OH + 2 M NaOH[a]	80	0.69	1.0	18.5	[33]
4 M bio-ethanol/H_2O solution[a]	80	0.80	0.033	21.4	[10]
10 wt% C_2H_5OH in 2 M KOH[b]	RT[c]	0.65–0.85	0.02–0.20	17.2–22.6	[72]
2 M C_2H_5OH + 2 M KOH[b]	25	0.70	0.125	19.2	This work

[a] Ion-exchange membrane was used in those electrolyzers. [b] Membrane-free electrolyzers. [c] Room temperature.

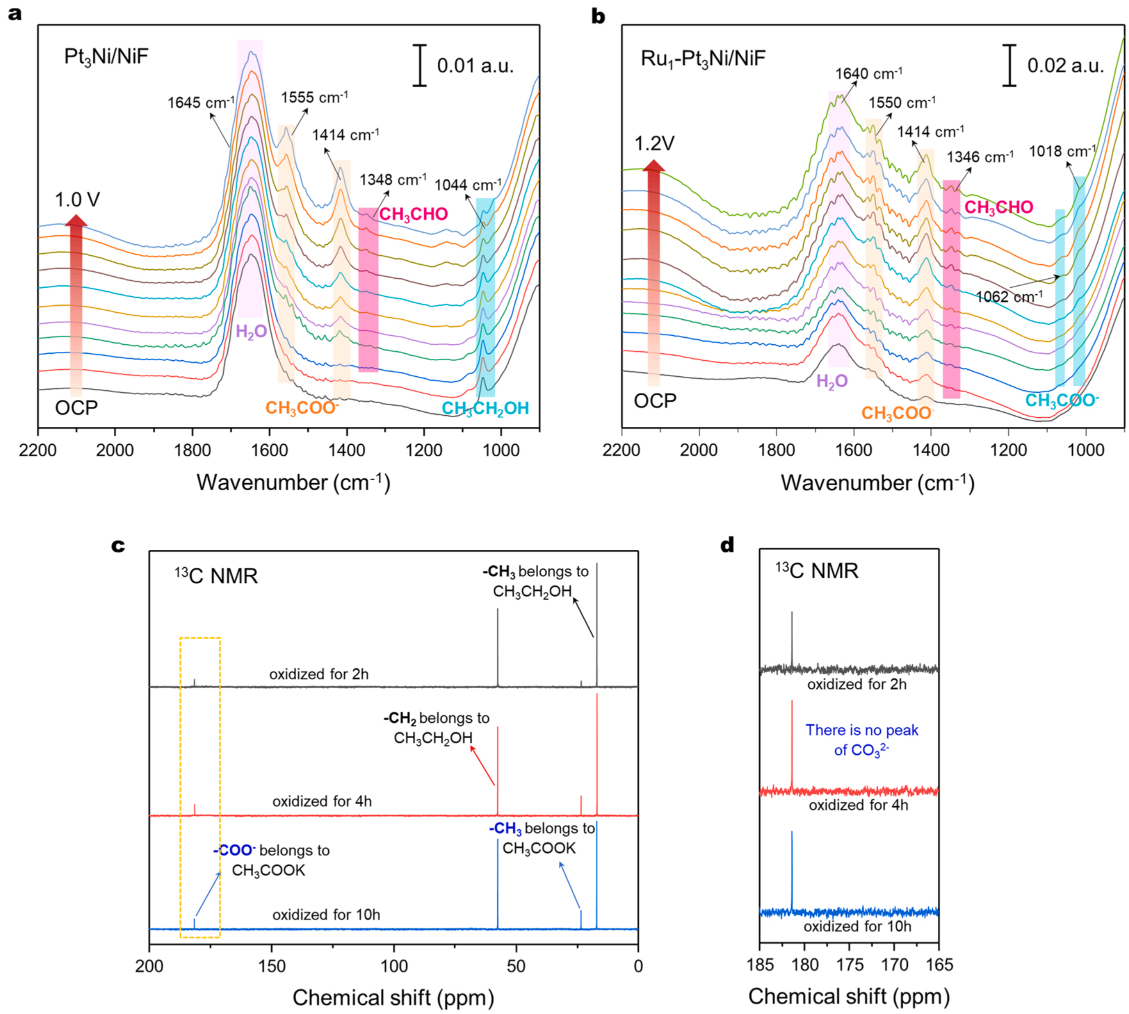

Fig. 4. In situ FTIR spectra recorded during chronoamperometry measurement from 0.1 V to 1.2 V (vs. RHE) for EOR at (a) Pt_3Ni/NiF and (b) Ru_1-Pt_3Ni/NiF catalysts. The data recording interval was 0.1 V. Electrolyte was N_2-saturated 1 M KOH with 1 M EtOH. All experiments were performed at 25 °C. (c) ^{13}C NMR spectra for oxidation products of ethanol at 0.6 V (vs. RHE) as a function of reaction time. (d) Amplified NMR spectra of carbonate characteristic region. In the enlarged spectra, no NMR signal was observed at the characteristic chemical shift of carbonate. It indicates that the concentration of carbonate in the reaction product is extremely low.

analyzed by C^{13} NMR. The chemical shifts of characteristic functional groups for possible EOR products are determined by standard samples C^{13} NMR spectra (Fig. S25). As shown in Fig. 4c, d, no obvious carbonate signal was detected in the products of ethanol oxidation (at 0.6 V vs. RHE) for 2, 4 and 10 h, respectively. The results shown in this work demonstrate that the catalysts promote the oxidation of ethanol in the alkaline electrolyte, mainly through the C2-pathway of $4e^-$ transfer, and the main oxidation product is acetic acid. The Ru_1-Pt_3Ni/NiF catalysts act out high selectivity for acetic acid pathway.

3.4. Operando XAS analysis of Ru_1-Pt_3Ni/NiF

To further understand the interaction of atomic dispersed Ru atoms and Pt_3Ni alloy in the Ru_1-Pt_3Ni/NiF catalyst regarding EOR activity and stability, operando XAS were implemented to investigate the electronic state and structural change during the electrochemical reaction process (Fig. 5a, S26). During the operando XANES measurement, the XAS spectrum was recorded under open-circuit potential (OCP), then the working electrode potential was increased to 0.2 V, 0.5 V vs. RHE, and the corresponding spectra were collected. As shown in Fig. 5b, the Pt L_3-edge absorption threshold and white line peak have no evident differences when the electrode potential increasing, suggesting that the oxidation state of Pt in the Ru_1-Pt_3Ni/NiF catalyst remains stable during EOR reaction. However, the absorption edge of Ru K-edge XANES shifts to higher energy and the intensity of white line increasing with the rising of applied potential, demonstrating that Ru was oxidized to higher valance state and there are convenient electron transfers between the single atomic Ru sites and electrolyte during EOR reaction (Fig. 5c). The dilution of electron density around Ru atom and the accumulation of electron density around O atom in Ru-OH structure revealed by differential charge density calculation also demonstrated the charge transfer phenomenon on Ru sites and the phenomenon of charge reconstruction becomes more obvious with the increase of adsorption OH around the Ru sites on the catalysts surface (Fig. S28). The oxygen affinity of ruthenium makes it easy to form surface adsorbed hydroxyl groups (OH*) [74]. The adsorbed OH (Ru-OH) has high oxidation ability, which can effectively oxidize the intermediate of EOR, indicates the active contribution of doped single Ru site for EOR performance. In addition, some researches show that the $Ru^{(4+\delta)+}$ species is an unstable phase in electrochemical circumstance, which will lead to the dissolution and degeneration of Ru species in Ru-based catalyst. Compared with the XANES spectrum of RuO_2 standard sample, it can be found that the oxidation state of Ru in Ru_1-Pt_3Ni/NiF catalyst is still below + 4 during the EOR process. That means the single atomic Ru site located on Pt_3Ni/NiF surface is stable under the working potential. Further FT-EXAFS studies show the intensity of scattering peak and scattering

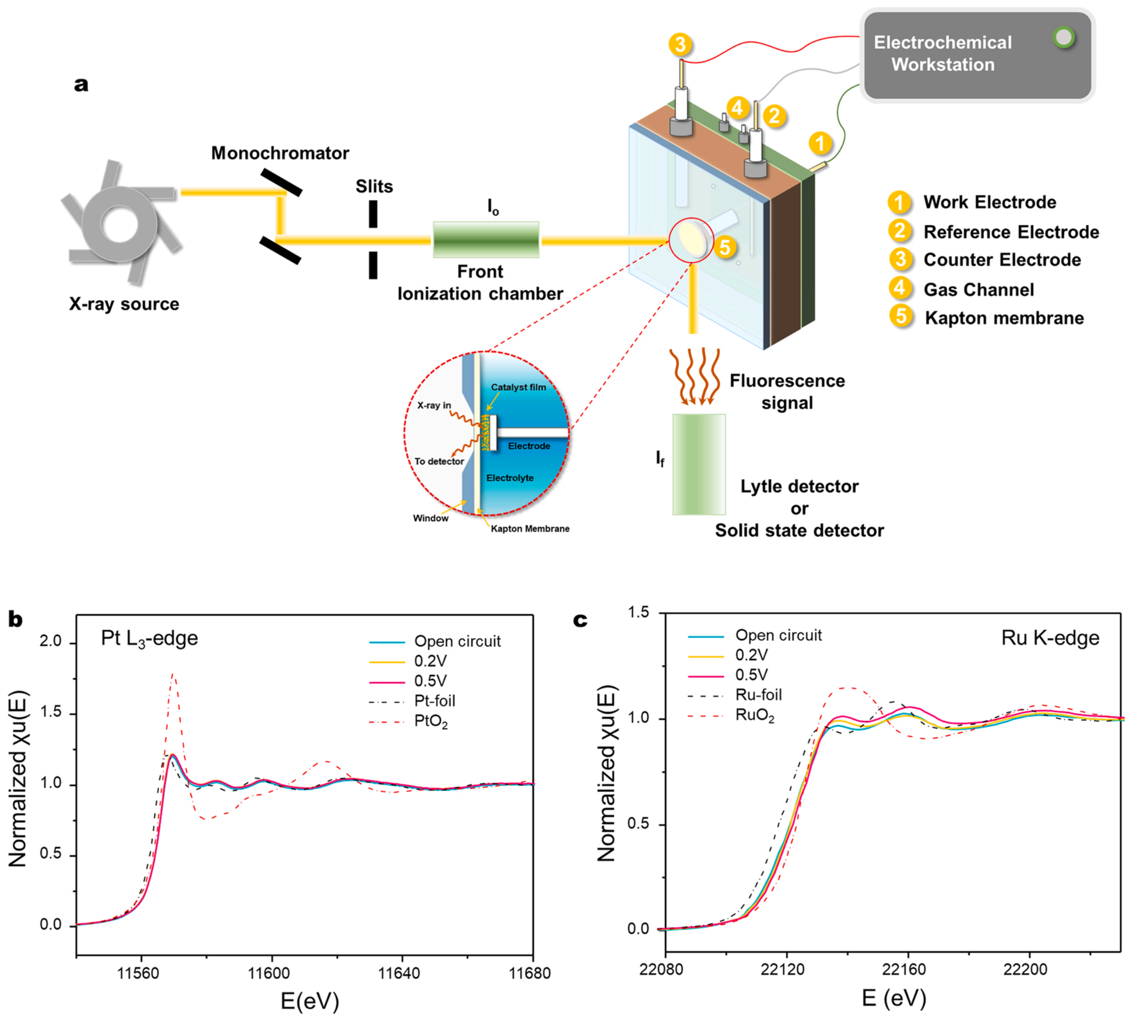

Fig. 5. The in-situ XAFS characterization of Ru_1-Pt_3Ni/NiF during EOR measured in 1 M KOH solutions within 1 M C_2H_5OH. XANES patterns of Ru_1-Pt_3Ni/NiF collected from (a) Pt L_3-edge and (b) Ru K-edge on different electrode potential, respectively.

path distance have no obvious change in Ru K-edge R space under different oxidation potentials, indicates the stable local structure of Ru atom in Ru_1-Pt_3Ni/NiF catalyst during EOR process (Fig. S27).

3.5. Mechanism of selective oxidation of ethanol

DFT calculations were performed to understand the high EOR electrocatalytic activity and C2 pathway selectivity of Ru_1-Pt_3Ni/NiF at atomic level. As shown in Fig. S29, similar with Pt (111), ethanol adsorbs relatively weakly on Pt site of Pt_3Ni (111) and Ru_1-Pt_3Ni (111) surface, with adsorption energies (ΔE_{ads}) of − 0.29, − 0.20 and − 0.19 eV, respectively. Ethanol adsorbs stronger on the Ru-doped Pt_3Ni (111) surface with ΔE_{ads} values of − 0.64 eV on single Ru atoms substituted in Pt_3Ni (111) facets of Pt site. Sufficient coverage of adsorbed OH species is necessary for ethanol oxidation [52], hence, the influence of Ru-doped on the formation of oxygen species (OH*) was also studied.

Gibbs free formation energy of hydroxyl (ΔG_{OH^*}) on different catalysts facets were presented in Fig. 6a. ΔG_{OH^*} on Pt (111), Pt site of Pt_3Ni (111), Ni site of Pt_3Ni (111), Pt site of Ru-doped Pt_3Ni (111) and Ru site of Ru-doped Pt_3Ni (111) was 0.30, 0.31, 0.21, 0.48 and − 0.36 eV, respectively. Doping Ru on Pt_3Ni (111) surface significantly reduced the formation barrier of hydroxyl groups on the surface of the catalyst. At the same time, ΔG_{OH^*} increased from 0.31 on Pt_3Ni (111) to 0.48 eV on Ru-doped Pt_3Ni (111), indicates that the formation of adsorbed hydroxyl on Pt sites on the Ru-doped Pt_3Ni (111) surface becomes more difficult. These findings indicate that doping Pt surfaces with Ru single atoms contribute in a stronger adsorption of ethanol and facile formation of OH*.

There is a consensus about the reaction mechanism of ethanol electro-oxidation that EOR proceeds via C1 and C2 pathways [43,45,75], cleavage of the C-C bond in the C1 pathway and acetaldehyde or acetic acid generated though C2 pathway. Neurock and co-workers have shown that most of the α-C-H and O-H scissions of ethanol oxidation network to acetic acid have lower barriers when assisted by co-adsorbed hydroxyl compared with the bare metal [76]. Due to the Ru doping, there are a lot of adsorbed hydroxyls on the surface of Ru_1-Pt_3Ni/NiF catalyst, which makes ethanol more facile to occur α-dehydrogenation and O-H bond breaking and result in CH_3CO^* intermediate, then the reaction of CH_3CO^* with adsorbed hydroxyls leads to CH_3COOH (Fig. 6b). The adsorption energies of acetic acid on different catalyst facets shown in Fig. 6c. The Ru doping weakens the interaction between acetic acid and Ru_1-Pt_3Ni (111) facets, from − 0.19 eV for Pt (111) to − 0.1 eV, which makes acetic acid easier to desorb and upon deprotonation gives acetate (CH_3COO^-). In addition, the surface structure affects significantly the reactivity of ethanol oxidation, the ability of C-C bond cleavage are known to increase in the order of Pt (111) < Pt (100) < < Pt (110), (111) surfaces were found to be inefficient at breaking C-C bonds [77], the activation barriers for the C-C bond breaking in CH_3CO and CH_2CO intermediates on Pt_3Ni (111) facets is still high compared

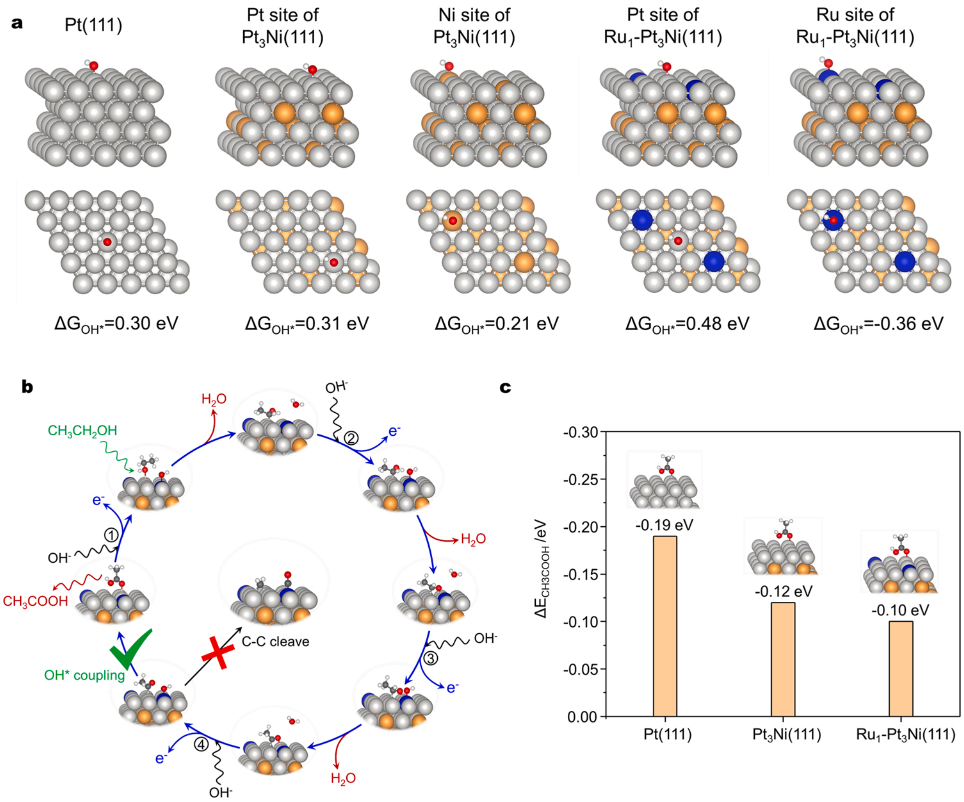

Fig. 6. (a) The adsorption configurations of surface hydroxyl on different catalysts facets and corresponding Gibbs free formation energy (ΔG_{OH^*}). (b) General reaction scheme based on ethanol C2 oxidation pathway. (c) Adsorption energies of CH_3COOH ($\Delta E_{CH3COOH}$) on different catalysts facets. Insets in panels are the corresponding adsorption structure.

with CH_3CO^* hydroxyl coupling. Obviously, these calculation results demonstrate that the single-atom Ru-tailored Pt_3Ni surface benefit the C2 pathway of the EOR. The CV profile for acetic acid did not show any oxidation current densities when deducting the background current densities, which is proof that the resulting acetate ($KOH + CH_3COOH$) is the end product during the ethanol C2 pathway electro-oxidation reaction (Fig. S30). To sum up, Ru doping enhanced the adsorption of ethanol and weakened the adsorption of acetic acid, due to the efficient adsorbed hydroxyl on Ru_1-Pt_3Ni surface, the α-dehydrogenation, O-H scissions and OH* coupling reactions are thermodynamics favor, which improves the activity and selectivity for C2 pathway of EOR.

4. Conclusions

In this study, monodisperse Ru-doped Pt_3Ni/Ni-foam catalysts were successful synthesized via galvanic spontaneous reduction induced by electronegativity, and the anodic selective ethanol oxidation was investigated on this catalyst. Thanks to Ru active sites introduced, charge transfer in the reaction interface was accelerated and enhanced electrocatalytic performances and durability for ethanol oxidation were achieved. More importantly, the Ru_1-Pt_3Ni/NiF catalysts exhibited excellent selectivity for acetic acid, acetate was the only electro-oxidation product detected. DFT calculations pointed out that Ru doping was conducive to the formation of OH* on Ru_1-Pt_3Ni/NiF, which makes the α-dehydrogenation, O-H scissions and OH* coupling reactions are thermodynamics favor, the selectivity of C2 pathway increased. By using Pt_3Ni/NiF as the HER catalyst and Ru_1-Pt_3Ni/NiF as the anodic catalyst, an overall membrane-free ethanol oxidation electrolyzer cell was built. Under 0.7 V cell voltage, continuous H_2 generation can be realized at 125 mA cm^{-2} current density, and the unit power consumption of hydrogen production is 19.24 kWh kg_{H2}^{-1}. This work provides a cost-competitive and energy-saving strategy for high-purity H_2 and value-added chemicals at room temperature, opening news opportunities for electric energy utilization from renewable sources.

CRediT authorship contribution statement

Chang-An Zhou: Conceptualization, Investigation, Methodology, Visualization, Writing – original draft, Writing – review & editing. **Shenghong Wang:** Resources, Validation. **Kui Ma:** Funding acquisition, Methodology, Formal analysis, Writing – review & editing. **Lei Song:** Methodology, Writing – review & editing. **Lirong Zheng:** Methodology, Software, Formal analysis. **Hairong Yue:** Funding acquisition, Supervision, Methodology, Writing – review & editing.

Declaration of Competing Interest

The authors declare that they have no known competing financial interests or personal relationships that could have appeared to influence the work reported in this paper.

Data Availability

Data will be made available on request.

Acknowledgements

The authors are grateful for the support from the National Natural Science Foundation of China (22078208, 22008160). We would like to thank Wen Tian from Center of Engineering Experimental Teaching, School of Chemical Engineering, Sichuan University for the help of FTIR spectrometer measurement. This work was carried out with the support of 1W1B beamline at Beijing Synchrotron Radiation Facility.The authors are gratefully thank the Institute of New Energy and Low-Carbon

Technology, Sichuan University, for XRD patterns acquisition work.

Appendix A. Supporting information

Supplementary data associated with this article can be found in the online version at doi:10.1016/j.apcatb.2022.122065.

References

[1] Y. Jiao, Y. Zheng, M. Jaroniec, S.Z. Qiao, Design of electrocatalysts for oxygen- and hydrogen-involving energy conversion reactions, Chem. Soc. Rev. 44 (2015) 2060–2086, https://doi.org/10.1039/C4CS00470A.

[2] I. Roger, M.A. Shipman, M.D. Symes, Earth-abundant catalysts for electrochemical and photoelectrochemical water splitting, Article 0003, Nat. Rev. Chem. 1 (2017), https://doi.org/10.1038/s41570-016-0003.

[3] X. Zou, Y. Zhang, Noble metal-free hydrogen evolution catalysts for water splitting, Chem. Soc. Rev. 44 (2015) 5148–5180, https://doi.org/10.1039/C4CS00448E.

[4] Y. Xu, B. Zhang, Recent advances in electrochemical hydrogen production from water assisted by alternative oxidation reactions, ChemElectroChem 6 (2019) 3214–3226, https://doi.org/10.1002/celc.201900675.

[5] L.-N. Zhang, Z.-L. Lang, Y.-H. Wang, H.-Q. Tan, H.-Y. Zang, Z.-H. Kang, Y.-G. Li, Cable-like Ru/WNO@C nanowires for simultaneous high-efficiency hydrogen evolution and low-energy consumption chlor-alkali electrolysis, Energy Environ. Sci. 12 (2019) 2569–2580, https://doi.org/10.1039/C9EE01647C.

[6] B. You, Y. Sun, Innovative strategies for electrocatalytic water splitting, Acc. Chem. Res. 51 (2018) 1571–1580, https://doi.org/10.1021/acs.accounts.8b00002.

[7] L. Chen, J. Shi, Chemical-assisted hydrogen electrocatalytic evolution reaction (CAHER), J. Mater. Chem. A 6 (2018) 13538–13548, https://doi.org/10.1039/C8TA03741H.

[8] B. You, G. Han, Y. Sun, Electrocatalytic and photocatalytic hydrogen evolution integrated with organic oxidation, Chem. Commun. 54 (2018) 5943–5955, https://doi.org/10.1039/C8CC01830H.

[9] F.M. Sapountzi, M.N. Tsampas, H.O.A. Fredriksson, J.M. Gracia, J. W. Niemantsverdriet, Hydrogen from electrochemical reforming of C1-C3 alcohols using proton conducting membranes, Int. J. Hydrog. Energy 42 (2017) 10762–10774, https://doi.org/10.1016/j.ijhydene.2017.02.195.

[10] A. Caravaca, A. de Lucas-Consuegra, A.B. Calcerrada, J. Lobato, J.L. Valverde, F. Dorado, From biomass to pure hydrogen: Electrochemical reforming of bio-ethanol in a PEM electrolyser, Appl. Catal. B 134–135 (2013) 302–309, https://doi.org/10.1016/j.apcatb.2013.01.033.

[11] D.-H. Nam, B.J. Taitt, K.-S. Choi, Copper-based catalytic anodes to produce 2,5-furandicarboxylic acid, a biomass-derived alternative to terephthalic acid, ACS Catal. 8 (2018) 1197–1206, https://doi.org/10.1021/acscatal.7b03152.

[12] B. You, X. Liu, N. Jiang, Y. Sun, A general strategy for decoupled hydrogen production from water splitting by integrating oxidative biomass valorization, J. Am. Chem. Soc. 138 (2016) 13639–13646, https://doi.org/10.1021/jacs.6b07127.

[13] B. You, X. Liu, X. Liu, Y. Sun, Efficient H_2 evolution coupled with oxidative refining of alcohols via a hierarchically porous nickel bifunctional electrocatalyst, ACS Catal. 7 (2017) 4564–4570, https://doi.org/10.1021/acscatal.7b00876.

[14] B. You, N. Jiang, X. Liu, Y. Sun, Simultaneous H_2 generation and biomass upgrading in water by an efficient noble-metal-free bifunctional electrocatalyst, Angew. Chem. Int. Ed. 55 (2016) 9913–9917, https://doi.org/10.1002/anie.201603798.

[15] Y. Huang, X. Chong, C. Liu, Y. Liang, B. Zhang, Boosting hydrogen production by anodic oxidation of primary amines over a NiSe nanorod electrode, Angew. Chem. Int. Ed. 57 (2018) 13163–13166, https://doi.org/10.1002/anie.201807717.

[16] J.-Y. Zhang, H. Wang, Y. Tian, Y. Yan, Q. Xue, T. He, H. Liu, C. Wang, Y. Chen, B. Y. Xia, Anodic hydrazine oxidation assists energy-efficient hydrogen evolution over a bifunctional cobalt perselenide nanosheet electrode, Angew. Chem. Int. Ed. 57 (2018) 7649–7653, https://doi.org/10.1002/anie.201803543.

[17] X. Wei, S. Wang, Z. Hua, L. Chen, J. Shi, Metal-organic framework nanosheet electrocatalysts for efficient H_2 production from methanol solution: methanol-assisted water splitting or methanol reforming? ACS Appl. Mater. Interfaces 10 (2018) 25422–25428, https://doi.org/10.1021/acsami.8b06948.

[18] L. Chen, X. Liang, X. Li, J. Pei, H. Lin, D. Jia, W. Chen, D. Wang, Y. Li, Promoting electrocatalytic methanol oxidation of platinum nanoparticles by cerium modification, Article 104784, Nano Energy 73 (2020), https://doi.org/10.1016/j.nanoen.2020.104784.

[19] H. Lei, X. Li, C. Sun, J. Zeng, S.S. Siwal, Q. Zhang, Galvanic replacement-mediated synthesis of Ni-supported Pd nanoparticles with strong metal-support interaction for methanol electro-oxidation, Article 1804722, Small 15 (2019), https://doi.org/10.1002/smll.201804722.

[20] J. Chang, L. Song, Y. Xu, Y. Ma, C. Liang, W. Jiang, Y. Zhang, Fishbone-like platinum-nickel nanowires as an efficient electrocatalyst for methanol oxidation, Nano Res. 13 (2020) 67–71, https://doi.org/10.1007/s12274-019-2573-7.

[21] L. Tao, Y. Shi, Y.-C. Huang, R. Chen, Y. Zhang, J. Huo, Y. Zou, G. Yu, J. Luo, C.-L. Dong, S. Wang, Interface engineering of Pt and CeO_2 nanorods with unique interaction for methanol oxidation, Nano Energy 53 (2018) 604–612, https://doi.org/10.1016/j.nanoen.2018.09.013.

[22] L. Dai, Q. Qin, X. Zhao, C. Xu, C. Hu, S. Mo, Y.O. Wang, S. Lin, Z. Tang, N. Zheng, Electrochemical partial reforming of ethanol into ethyl acetate using ultrathin Co_3O_4 nanosheets as a highly selective anode catalyst, ACS Cent. Sci. 2 (2016) 538–544, https://doi.org/10.1021/acscentsci.6b00164.

[23] A. Caravaca, F.M. Sapountzi, A. de Lucas-Consuegra, C. Molina-Mora, F. Dorado, J. L. Valverde, Electrochemical reforming of ethanol-water solutions for pure H_2 production in a PEM electrolysis cell, Int. J. Hydrog. Energy 37 (2012) 9504–9513, https://doi.org/10.1016/j.ijhydene.2012.03.062.

[24] A. Rodríguez-Gómez, F. Dorado, A. de Lucas-Consuegra, A.R. de la Osa, Influence of Pt/Ru anodic ratio on the valorization of ethanol by PEM electrocatalytic reforming towards value-added products, J. Energy Chem. 56 (2021) 264–275, https://doi.org/10.1016/j.jechem.2020.07.061.

[25] Y. Ding, Q. Xue, Q.-L. Hong, F.-M. Li, Y.-C. Jiang, S.-N. Li, Y. Chen, Hydrogen and potassium acetate co-production from electrochemical reforming of ethanol at ultrathin cobalt sulfide nanosheets on nickel foam, ACS Appl. Mater. Interfaces 13 (2021) 4026–4033, https://doi.org/10.1021/acsami.0c20554.

[26] F. Guo, Y. Li, B. Fan, Y. Liu, L. Lu, Y. Lei, Carbon- and binder-free core-shell nanowire arrays for efficient ethanol electro-oxidation in alkaline medium, ACS Appl. Mater. Interfaces 10 (2018) 4705–4714, https://doi.org/10.1021/acsami.7b16615.

[27] B.-W. Zhang, T. Sheng, Y.-X. Wang, X.-M. Qu, J.-M. Zhang, Z.-C. Zhang, H.-G. Liao, F.-C. Zhu, S.-X. Dou, Y.-X. Jiang, S.-G. Sun, Platinum-cobalt bimetallic nanoparticles with Pt skin for electro-oxidation of ethanol, ACS Catal. 7 (2017) 892–895, https://doi.org/10.1021/acscatal.6b03021.

[28] E. Leal da Silva, A. Cuña, M. Rita Ortega Vega, C. Radtke, G. Machado, N. Tancredi, C. de Fraga Malfatti, Influence of the support on PtSn electrocatalysts behavior: ethanol electro-oxidation performance and in-situ ATR-FTIRS studies, Appl. Catal. B 193 (2016) 170–179, https://doi.org/10.1016/j.apcatb.2016.04.021.

[29] T. Öznülüer, Ü. Demir, H. Öztürk Doğan, Fabrication of underpotentially deposited Cu monolayer/electrochemically reduced graphene oxide layered nanocomposites for enhanced ethanol electro-oxidation, Appl. Catal. B 235 (2018) 56–65, https://doi.org/10.1016/j.apcatb.2018.04.065.

[30] W.J. Pech-Rodríguez, D. González-Quijano, G. Vargas-Gutiérrez, C. Morais, T. W. Napporn, F.J. Rodríguez-Varela, Electrochemical and in situ FTIR study of the ethanol oxidation reaction on PtMo/C nanomaterials in alkaline media, Appl. Catal. B 203 (2017) 654–662, https://doi.org/10.1016/j.apcatb.2016.10.058.

[31] L. Chen, L. Lu, H. Zhu, Y. Chen, Y. Huang, Y. Li, L. Wang, Improved ethanol electrooxidation performance by shortening Pd-Ni active site distance in Pd-Ni-P nanocatalysts, Article 14136, Nat. Commun., 8 (2017), https://doi.org/10.1038/ncomms14136.

[32] Y. Zhao, S. Xing, X. Meng, J. Zeng, S. Yin, X. Li, Y. Chen, Ultrathin Rh nanosheets as a highly efficient bifunctional electrocatalyst for isopropanol-assisted overall water splitting, Nanoscale 11 (2019) 9319–9326, https://doi.org/10.1039/C9NR02153A.

[33] Y.X. Chen, A. Lavacchi, H.A. Miller, M. Bevilacqua, J. Filippi, M. Innocenti, A. Marchionni, W. Oberhauser, L. Wang, F. Vizza, Nanotechnology makes biomass electrolysis more energy efficient than water electrolysis, Article 4036, Nat. Commun. 5 (2014), https://doi.org/10.1038/ncomms5036.

[34] A.T. Marshall, R.G. Haverkamp, Production of hydrogen by the electrochemical reforming of glycerol-water solutions in a PEM electrolysis cell, Int. J. Hydrog. Energy 33 (2008) 4649–4654, https://doi.org/10.1016/j.ijhydene.2008.05.029.

[35] J. Zheng, X. Chen, X. Zhong, S. Li, T. Liu, G. Zhuang, X. Li, S. Deng, D. Mei, J.-G. Wang, Hierarchical porous NC@CuCo nitride nanosheet networks: highly efficient bifunctional electrocatalyst for overall water splitting and selective electrooxidation of benzyl alcohol, Article 1704169, Adv. Funct. Mater. 27 (2017), https://doi.org/10.1002/adfm.201704169.

[36] Z. Xu, L. Rao, H. Song, Z. Yan, L. Zhang, S. Yang, Enhanced ethanol electro-oxidation on CeO_2-modified Pt/Ni catalysts in alkaline solution, Chin. J. Catal. 38 (2017) 305–312, https://doi.org/10.1016/S1872-2067(16)62560-3.

[37] M.J.S. Farias, W. Cheuquepán, A.A. Tanaka, J.M. Feliu, Identity of the most and least active sites for activation of the pathways for CO_2 formation from the electro-oxidation of methanol and ethanol on platinum, ACS Catal. 10 (2020) 543–555, https://doi.org/10.1021/acscatal.9b04275.

[38] J.W. Magee, W.-P. Zhou, M.G. White, Promotion of Pt surfaces for ethanol electro-oxidation by the addition of small SnO_2 nanoparticles: activity and mechanism, Appl. Catal. B 152–153 (2014) 397–402, https://doi.org/10.1016/j.apcatb.2014.01.057.

[39] T. Sheng, C. Qiu, X. Lin, W.-F. Lin, S.-G. Sun, Insights into ethanol electro-oxidation over solvated Pt(100): origin of selectivity and kinetics revealed by DFT, Article 147505, Appl. Surf. Sci. 533 (2020), https://doi.org/10.1016/j.apsusc.2020.147505.

[40] D. Chu, J. Wang, S. Wang, L. Zha, J. He, Y. Hou, Y. Yan, H. Lin, Z. Tian, High activity of Pd-In_2O_3/CNTs electrocatalyst for electro-oxidation of ethanol, Catal. Commun. 10 (2009) 955–958, https://doi.org/10.1016/j.catcom.2008.12.041.

[41] T. Wu, Y. Ma, Z. Qu, J. Fan, Q. Li, P. Shi, Q. Xu, Y. Min, Black phosphorus-graphene heterostructure-supported Pd nanoparticles with superior activity and stability for ethanol electro-oxidation, ACS Appl. Mater. Interfaces 11 (2019) 5136–5145, https://doi.org/10.1021/acsami.8b20240.

[42] M. Yang, M. Pang, J. Chen, F. Gao, H. Li, P. Guo, Surfactant-assisted synthesis of palladium nanosheets and nanochains for the electrooxidation of ethanol, ACS Appl. Mater. Interfaces 13 (2021) 9830–9837, https://doi.org/10.1021/acsami.0c20146.

[43] E.A. Monyoncho, S.N. Steinmann, C. Michel, E.A. Baranova, T.K. Woo, P. Sautet, Ethanol electro-oxidation on palladium revisited using polarization modulation infrared reflection absorption spectroscopy (PM-IRRAS) and density functional theory (DFT): Why is it difficult to break the C-C Bond? ACS Catal. 6 (2016) 4894–4906, https://doi.org/10.1021/acscatal.6b00289.

[44] L.S.R. Silva, C.V.S. Almeida, C.T. Meneses, E.A. Batista, S.F. Santos, K.I.B. Eguiluz, G.R. Salazar-Banda, AuPd/C core-shell and alloy nanoparticles with enhanced catalytic activity toward the electro-oxidation of ethanol in alkaline media, Appl. Catal. B 251 (2019) 313–325, https://doi.org/10.1016/j.apcatb.2019.03.067.

[45] S. Luo, L. Zhang, Y. Liao, L. Li, Q. Yang, X. Wu, X. Wu, D. He, C. He, W. Chen, Q. Wu, M. Li, E.J.M. Hensen, Z. Quan, A tensile-strained Pt-Rh single-atom alloy remarkably boosts ethanol oxidation, Article 2008508, Adv. Mater. 33 (2021), https://doi.org/10.1002/adma.202008508.

[46] N.-F. Yu, N. Tian, Z.-Y. Zhou, L. Huang, J. Xiao, Y.-H. Wen, S.-G. Sun, Electrochemical synthesis of tetrahexahedral rhodium nanocrystals with extraordinarily high surface energy and high electrocatalytic activity, Angew. Chem. Int. Ed. 53 (2014) 5097–5101, https://doi.org/10.1002/anie.201310597.

[47] Q. Chang, S. Kattel, X. Li, Z. Liang, B.M. Tackett, S.R. Denny, P. Zhang, D. Su, J. G. Chen, Z. Chen, Enhancing C-C bond scission for efficient ethanol oxidation using PtIr nanocube electrocatalysts, ACS Catal. 9 (2019) 7618–7625, https://doi.org/10.1021/acscatal.9b02039.

[48] J. Bai, D. Liu, J. Yang, Y. Chen, Nanocatalysts for electrocatalytic oxidation of ethanol, ChemSusChem 12 (2019) 2117–2132, https://doi.org/10.1002/cssc.201803063.

[49] Y. Liu, M. Wei, D. Raciti, Y. Wang, P. Hu, J.H. Park, M. Barclay, C. Wang, Electro-oxidation of ethanol using Pt_3Sn alloy nanoparticles, ACS Catal. 8 (2018) 10931–10937, https://doi.org/10.1021/acscatal.8b03763.

[50] J.E. Sulaiman, S. Zhu, Z. Xing, Q. Chang, M. Shao, Pt-Ni octahedra as electrocatalysts for the ethanol electro-oxidation reaction, ACS Catal. 7 (2017) 5134–5141, https://doi.org/10.1021/acscatal.7b01435.

[51] L. Zhang, K. Doyle-Davis, X. Sun, Pt-based electrocatalysts with high atom utilization efficiency: from nanostructures to single atoms, Energy Environ. Sci. 12 (2019) 492–517, https://doi.org/10.1039/C8EE02939C.

[52] H. Mistry, A.S. Varela, S. Kühl, P. Strasser, B.R. Cuenya, Nanostructured electrocatalysts with tunable activity and selectivity, Article 16009, Nat. Rev. Mater. 1 (2016), https://doi.org/10.1038/natrevmats.2016.9.

[53] V. Del Colle, A. Berná, G. Tremiliosi-Filho, E. Herrero, J.M. Feliu, Ethanol electrooxidation onto stepped surfaces modified by Ru deposition: electrochemical and spectroscopic studies, Phys. Chem. Chem. Phys. 10 (2008) 3766–3773, https://doi.org/10.1039/B802683A.

[54] A. Lasia, A. Rami, Kinetics of hydrogen evolution on nickel electrodes, J. Electroanal. Chem. Interfacial Electrochem 294 (1990) 123–141, https://doi.org/10.1016/0022-0728(90)87140-F.

[55] P. Gu, L. Bai, L. Gao, R. Brousseau, B.E. Conway, Problems in the determination of adsorption behaviour of intermediates in faradaic reactions: Distinction between double layer and adsorption capacitance of electrocatalysts determined from fast potential relaxation transients, Electrochim. Acta 37 (1992) 2145–2154, https://doi.org/10.1016/0013-4686(92)85105-T.

[56] E.G. Gagnon, The triangular voltage sweep method for determining double-Layer capacity of porous electrodes, Article 512, J. Electrochem. Soc. 121 (1974), https://doi.org/10.1149/1.2401846.

[57] S. Iseki, K. Ohashi, S. Nagaura, Impedance of the oxygen-evolution reaction on noble metal electrodes, Electrochim. Acta 17 (1972) 2249–2265, https://doi.org/10.1016/0013-4686(72)87016-6.

[58] L. Bai, L. Gao, B.E. Conway, Problem of in situ real-area determination in evaluation of performance of rough or porous, gas-evolving electrocatalysts. Part 2.-Unfolding of the electrochemically accessible surface of rough or porous electrodes: a case-study with an electrodeposited porous Pt electrode, J. Chem. Soc., Faraday Trans. 89 (1993) 243–249, https://doi.org/10.1039/FT9938900243.

[59] G. Kresse, J. Furthmüller, Efficient iterative schemes for ab initio total-energy calculations using a plane-wave basis set, Phys. Rev. B 54 (1996) 11169–11186, https://doi.org/10.1103/PhysRevB.54.11169.

[60] G. Kresse, J. Hafner, Ab initio molecular dynamics for liquid metals, Phys. Rev. B 47 (1993) 558–561, https://doi.org/10.1103/PhysRevB.47.558.

[61] P.E. Blöchl, Projector augmented-wave method, Phys. Rev. B 50 (1994) 17953–17979, https://doi.org/10.1103/PhysRevB.50.17953.

[62] H.G. Manning, S. Biswas, J.D. Holmes, J.J. Boland, Nonpolar resistive switching in $Ag@TiO_2$ core-shell nanowires, ACS Appl. Mater. Interfaces 9 (2017) 38959–38966, https://doi.org/10.1021/acsami.7b10666.

[63] V. Wang, N. Xu, J. Liu, G. Tang, W. Geng, VASPKIT: A user-friendly interface facilitating high-throughput computing and analysis using VASP code, Article 108033, Comput. Phys. Commun. 267 (2021), https://doi.org/10.1016/j.cpc.2021.108033.

[64] S. Uhm, H. Jeon, T.J. Kim, J. Lee, Clean hydrogen production from methanol-water solutions via power-saved electrolytic reforming process, J. Power Sources 198 (2012) 218–222, https://doi.org/10.1016/j.jpowsour.2011.09.083.

[65] S.P. Sethu, S. Gangadharan, S.H. Chan, U. Stimming, Development of a novel cost effective methanol electrolyzer stack with Pt-catalyzed membrane, J. Power Sources 254 (2014) 161–167, https://doi.org/10.1016/j.jpowsour.2013.12.103.

[66] H. Ju, S. Giddey, S.P.S. Badwal, The role of nanosized SnO_2 in Pt-based electrocatalysts for hydrogen production in methanol assisted water electrolysis, Electrochim. Acta 229 (2017) 39–47, https://doi.org/10.1016/j.electacta.2017.01.106.

[67] C. Lamy, T. Jaubert, S. Baranton, C. Coutanceau, Clean hydrogen generation through the electrocatalytic oxidation of ethanol in a proton exchange membrane electrolysis Cell (PEMEC): Effect of the nature and structure of the catalytic anode, J. Power Sources 245 (2014) 927–936, https://doi.org/10.1016/j.jpowsour.2013.07.028.

[68] H. Ju, S. Giddey, S.P.S. Badwal, R.J. Mulder, Electro-catalytic conversion of ethanol in solid electrolyte cells for distributed hydrogen generation, Electrochim. Acta 212 (2016) 744–757, https://doi.org/10.1016/j.electacta.2016.07.062.

[69] A.R. de la Osa, A.B. Calcerrada, J.L. Valverde, E.A. Baranova, A. de Lucas-Consuegra, Electrochemical reforming of alcohols on nanostructured platinum-tin catalyst-electrodes, Appl. Catal. B 179 (2015) 276–284, https://doi.org/10.1016/j.apcatb.2015.05.026.

[70] H.A. Miller, M. Bellini, F. Vizza, C. Hasenöhrl, R.D. Tilley, Carbon supported Au-Pd core-shell nanoparticles for hydrogen production by alcohol electroreforming, Catal. Sci. Technol. 6 (2016) 6870–6878, https://doi.org/10.1039/C6CY00720A.

[71] M.V. Pagliaro, M. Bellini, M. Bevilacqua, J. Filippi, M.G. Folliero, A. Marchionni, H.A. Miller, W. Oberhauser, S. Caporali, M. Innocenti, F. Vizza, Carbon supported Rh nanoparticles for the production of hydrogen and chemicals by the electroreforming of biomass-derived alcohols, RSC Adv. 7 (2017) 13971–13978, https://doi.org/10.1039/C7RA00044H.

[72] V. Bambagioni, M. Bevilacqua, C. Bianchini, J. Filippi, A. Lavacchi, A. Marchionni, F. Vizza, P.K. Shen, Self-sustainable production of hydrogen, chemicals, and energy from renewable alcohols by electrocatalysis, ChemSusChem 3 (2010) 851–855, https://doi.org/10.1002/cssc.201000103.

[73] A.O. Neto, J. Nandenha, M.H.M.T. Assumpção, M. Linardi, E.V. Spinacé, R.F.B. de Souza, In situ spectroscopy studies of ethanol oxidation reaction using a single fuel cell/ATR-FTIR setup, Int. J. Hydrog. Energy 38 (2013) 10585–10591, https://doi.org/10.1016/j.ijhydene.2013.06.026.

[74] Y. Dang, T. Wu, H. Tan, J. Wang, C. Cui, P. Kerns, W. Zhao, L. Posada, L. Wen, S. L. Suib, Partially reduced Ru/RuO_2 composites as efficient and pH-universal electrocatalysts for hydrogen evolution, Energy Environ. Sci. 14 (2021) 5433–5443, https://doi.org/10.1039/D1EE02380B.

[75] T. Sheng, W.-F. Lin, S.-G. Sun, Elucidation of the surface structure-selectivity relationship in ethanol electro-oxidation over platinum by density functional theory, Phys. Chem. Chem. Phys. 18 (2016) 15501–15504, https://doi.org/10.1039/C6CP02484J.

[76] D.D. Hibbitts, M. Neurock, Influence of oxygen and pH on the selective oxidation of ethanol on Pd catalysts, J. Catal. 299 (2013) 261–271, https://doi.org/10.1016/j.jcat.2012.11.016.

[77] F. Colmati, G. Tremiliosi-Filho, E.R. Gonzalez, A. Berná, E. Herrero, J.M. Feliu, Surface structure effects on the electrochemical oxidation of ethanol on platinum single crystal electrodes, Faraday Discuss. 140 (2009) 379–397, https://doi.org/10.1039/B802160K.